A&A, 684, A68 (2024)
https://doi.org/10.1051/0004-6361/202348257

Astronomy & Astrophysics

Indication of a fast ejecta fragment in the atomic cloud interacting with the southwestern limb of SN 1006

R. Giuffrida[1,2], M. Miceli[1,2], S. Ravikularaman[3], V. H. M. Phan[4,5], S. Gabici[3], P. Mertsch[5], S. Orlando[2], and F. Bocchino[2]

[1] Dipartimento di Fisica e Chimica E. Segrè, Università degli Studi di Palermo, Piazza del Parlamento 1, 90134 Palermo, Italy
[2] INAF – Osservatorio Astronomico di Palermo, Piazza del Parlamento 1, 90134 Palermo, Italy
e-mail: roberta.giuffrida@inaf.it
[3] Université de Paris, CNRS, Astroparticule et Cosmologie, 75013 Paris, France
[4] Sorbonne Université, Observatoire de Paris, PSL Research University, LERMA, CNRS UMR 8112, 75005 Paris, France
[5] Institute for Theoretical Particle Physics and Cosmology (TTK), RWTH Aachen University, 52056 Aachen, Germany

Received 12 October 2023 / Accepted 9 January 2024

ABSTRACT

Context. Supernova remnants interacting with molecular and atomic clouds are interesting X-ray sources for studies of broadband nonthermal emission. X-ray line emission in these systems can be produced by different processes, such as low-energy cosmic rays (LECRs) interacting with the cloud and fast ejecta fragments moving in the cloud.
Aims. This paper is aimed at studying the origin of the non-thermal X-ray emission of the southwestern limb of SN 1006 beyond the main shock to determine whether the emission is due to LECRs diffusing in the cloud or to ejecta knots moving into the cloud.
Methods. We analyzed the X-ray emission of the southwestern limb of SN 1006, where the remnant interacts with an atomic cloud, using three different X-ray telescopes: *NuSTAR*, *Chandra*, and *XMM-Newton*. We also performed a combined spectro-imaging analysis of this region.
Results. Our analysis of the nonthermal X-ray emission of the southwestern limb of SN 1006 interacting with an atomic cloud has led to the detection of an extended X-ray source in the atomic cloud, approximately 2 pc upstream of the shock front. The source is characterized by a hard continuum (described by a power law with photon index $\Gamma \sim 1.4$) and by Ne, Si, and Fe emission lines. The observed flux suggests that the origin of the X-ray emission is not associated with LECRs interacting with the cloud. On the other hand, the spectral properties of the source, together with the detection of an IR counterpart visible with *Spitzer*-MIPS at 24 μm, are in good agreement with the general expectations for a fast ejecta fragment moving within the atomic cloud.
Conclusions. We detected X-ray and IR emission from a possible ejecta fragment, with an approximate radius of 1×10^{17} cm and approximate mass of $10^{-3}\ M_{\odot}$ at about 2 pc out of the shell of SN 1006, in the interaction region between the southwestern limb of the remnant and the atomic cloud.

Key words. ISM: supernova remnants – X-rays: ISM – X-rays: individuals: SN 1006

1. Introduction

Supernovaremnants (SNRs) that interact with interstellar clouds are interesting sources of broadband nonthermal emission. In addition to the characteristic hadronic γ-ray emission associated with π^0 decay and the OH maser emission in radio, nonthermal X-rays are also expected.

Different processes can lead to nonthermal continuum and line emission in X-rays. The bulk of the continuum X-ray emission is typically associated with synchrotron radiation from secondary electrons, the products of $\pi^{\pm}$ decays produced in the interaction of cosmic rays diffusing from the SNR in the nearby cloud, while bremsstrahlung emission from primary and secondary electrons can play an important role in the very hard part of the X-ray band (e.g., Gabici et al. 2009).

Nonthermal line emission is also expected. Tatischeff et al. (2012) have shown that low-energy cosmic rays (LECRs) interacting with the dense interstellar medium (ISM) can produce the characteristic Fe Kα emission line at 6.4 keV, observed in the X-ray spectra of the Arches cluster region, near the Galactic center. This phenomenon can be expected also in supernova remnants interacting with Molecular Clouds (MCs, e.g., Gabici 2022). Nobukawa et al. (2019) revealed the presence of two localized regions with enhanced Fe I Kα line emission in the northern and central part of IC 443, where the remnant is interacting with extremely dense MCs (e.g., Cosentino et al. 2022). This detection was explained as the result of protons at MeV energies accelerated in the SNR and diffusing into the cloud. These particles can eject inner-shell electrons of neutral iron atoms in the cloud, thus producing the Kα line emission. A similar scenario can be invoked for the Fe Kα emission detected in the region where the SNR W28 is interacting with a MC, as reported by Okon et al. (2018) and by Nobukawa et al. (2018; though the two works report enhanced emission in different parts of the remnant). The Fe emission line is consistent with being produced by LECRs, as shown by Phan et al. (2020), who also demonstrated that the enhanced ionization rate in regions near W28 is due to cosmic-ray protons.

Nonthermal X-ray emission in MCs interacting with SNRs can also be observed when fast moving ejecta fragments propagate in the cloud. A theoretical model developed by Bykov (2002, hereafter B02) shows that ejecta knots can produce X-ray

nonthermal (continuum and line) emission when interacting with the ISM. The supersonic motion of the ejecta produces a radiative bow shock with prominent infrared (IR) emission. Nonthermal electrons accelerated at the bow-shock diffuse in the fragment, suffering from Coulomb losses and ionizing neutral atoms in the cold clump, thus producing K-shell emission. B02 shows that the line emission increases with the density of the medium, being high when the ejecta knots propagate in MCs. Clear indications strongly supporting this scenario have been obtained by detecting small (albeit extended) hard X-ray emitting sources in IC 443 (Bocchino & Bykov 2003; Bykov 2003; Bykov et al. 2005; Zhang et al. 2018) and Kes 69 (Bocchino et al. 2012).

SN 1006 is a Type Ia SNR located well above the galactic plane (~550 pc, at a distance of 2.2 kpc, Winkler et al. 2003). Its evolution in a tenuous ISM with density $n_0 \sim 0.04\,\mathrm{cm}^{-3}$ (Miceli et al. 2012; Giuffrida et al. 2022) makes it a dynamically young remnant. The shock velocity is of the order of $5000\,\mathrm{km\,s}^{-1}$, although lower velocities are observed in the northwest and in a local indentation of the southwestern shock most likely due to interaction with a denser environment (Katsuda et al. 2009; Winkler et al. 2014; Miceli et al. 2016). The remnant presents a characteristic nonthermal bilateral emission, with two opposite bright limbs (at northeast and southwest) clearly visible in X-rays, but also in the radio (Petruk et al. 2009) and γ-ray band, (Acero et al. 2010). Thermal X-ray emission, mainly associated with ejecta knots, is observed in the northeast, northwest, and toward the center.

Despite evolving in a fairly uniform ambient medium, the decrease of the shock velocity shows that two regions of SN 1006 interact with atomic clouds, namely, in the northwest and southwest (see Fig. 1). The interaction with an atomic cloud in the northwestern part of the remnant was well studied with multiwavelength observations (e.g., Long et al. 1988; Dubner et al. 2002; Korreck et al. 2004; Raymond et al. 2007; Acero et al. 2007; Katsuda et al. 2013) and is associated with a clearly visible Hα filament (e.g., Winkler et al. 2014). The interaction of the southwestern part of SN 1006 with an atomic cloud was studied with radio and X-ray observations (Miceli et al. 2014) and modeled with MHD simulations (Miceli et al. 2016). The combined analysis of X-ray and radio data indicates that the core of the cloud has a density of the order of $n_{\mathrm{core}} \sim 10\,\mathrm{cm}^{-3}$ (Miceli et al. 2014, see also Fig. 1). On the other hand, the comparison of the observations with a detailed 3D MHD model, clearly indicates that the part of the cloud actually interacting with the remnant has a density $n_{\mathrm{cl}} \sim 0.5\,\mathrm{cm}^{-3}$ (Miceli et al. 2016).

Recently, a thorough analysis of X-ray observations showed that SN 1006 can accelerate efficiently both electrons and protons in its nonthermal limbs (Giuffrida et al. 2022). In particular, the efficient hadron acceleration in quasi-parallel conditions (i.e., when the shock normal is almost aligned with the ambient magnetic field) modifies the shock structure, and the shock compression ratio deviates significantly from the canonical value of 4, increasing up to ~7 in the nonthermal limbs (Miceli et al. 2012; Giuffrida et al. 2022). The inferred azimuthal profile of the compression ratio is in agreement with that expected for modified shocks including the effects of the shock postcursor (Haggerty & Caprioli 2020; Caprioli et al. 2020).

The southwestern limb of SN 1006 is then characterized by shock-cloud interaction and efficient acceleration of cosmic rays. We then expect the southwestern cloud to be a promising source of nonthermal X-rays, which may be associated with LECRs diffusing from the shock to the cloud. On the other hand, nonthermal X-ray emission might be also associated with fast moving ejecta knots decelerating in the cloud.

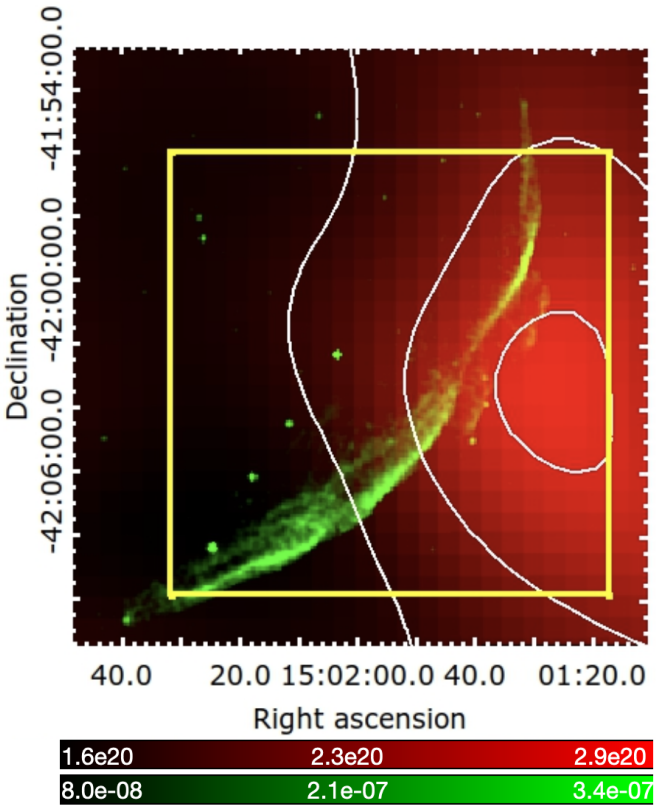

Fig. 1. *Chandra* flux map of SN 1006 in count $\mathrm{s}^{-1}\,\mathrm{cm}^{-2}$ in the 2.5–7 keV (green) band. The column density of HI in the [+5.8, +10.7] $\mathrm{km\,s}^{-1}$ velocity range is shown in red. The contour levels of the column density at the 65%, 80% and 95% of the maximum ($2.9 \times 10^{20}\,\mathrm{cm}^{-2}$) are shown in white. The yellow rectangle shows the *NuSTAR* field of view.

This paper presents the analysis of different archival X-ray observations (performed with *NuSTAR*, *XMM-Newton* and *Chandra*) of the southwestern region of SN 1006, where we revealed a small (≈3″) extended source of nonthermal X-rays (with an IR counterpart, detected with *Spitzer*), located beyond the shell of the remnant, within the atomic cloud.

The paper is organized as follows. In Sect. 2, we describe the data reduction procedure. Section 3 shows the results of our image and spectral analysis. Section 4 is dedicated to the discussion on the origin of the nonthermal (and IR) emission. Finally, in Sect. 5, we draw our conclusion.

2. Data reduction

Here, we analyze observations of the southwestern limb of SN 1006 performed with *NuSTAR* (FPMA, FPMB; Li et al. 2018), *XMM-Newton*/EPIC, *Chandra*/ACIS, and *Spitzer*/MIPS (Winkler et al. 2003). Table 1 summarizes the relevant information about the data.

Data were reprocessed according to the process detailed below. The *NuSTAR* data analysis was performed with the *NuSTAR* Data Analysis Software, NuSTARDAS, version 1.2.0 with CALDB version 4.9.4 within HEAsoft version v6.28. The data were reprocessed with `nupipeline`. Spectra were extracted by using the `nuproduct` pipeline, which also generates the corresponding ancillary response file (arf) and redistribution

Table 1. Observations analyzed in this work.

Telescope	OBS ID	Camera	PI	α	δ	T_{exp} (ks)	Start date
NuSTAR	40110002002	FPMA/FPMB	J. Li	15h 01m 49.6s	−42° 02′ 47″	204.712	2016-03-8
XMM-Newton	0653860101	EPIC-MOS1 [(a)]	A. Decourchelle	15h 02m 06.00s	−42° 05′ 26.0″	99.578/130.07 [(b)]	2010-08-28
		EPIC-MOS2 [(a)]				101.967/130.070 [(b)]	
		EPIC-pn [(a)]				71.623/130.070 [(b)]	
Chandra (2003)	4386	ACIS-I	Hughes	15h 02m 07.01s	−42° 07′ 30.00″	20	2003-04-09
Chandra (2012)	13738	ACIS-I	P. F. Winkler	15h 01m 41.78s	−41° 58′ 14.96″	73.47	2012-04-23
	14424	ACIS-I	P. F. Winkler	15h 01m 41.78s	−41° 58′ 14.96″	25.39	2012-04-27
Spitzer	30673 [(c)]	MIPS	P. F. Winkler	15h 01m 54.00s	−41° 53′ 00.0″	10.383	2007-08-22
	30673 [(d)]	MIPS	P. F. Winkler	15h 01m 40.00s	−41° 51′ 00.0″	17.590	2007-03-05

Notes. All the important information of each observation are included. [(a)]EPIC-MOS1/MOS2 cameras are in Full Frame Window mode, EPIC-pn camera in Extended Full Frame mode. [(b)]Screened/unscreened exposure time. [(c)]AOR: 18725376. [(d)]AOR: 18725120.

matrix (rmf). FPMA and FPMB spectra were fitted simultaneously. The *XMM-Newton* data were reprocessed with the Science Analysis System (SAS v 19.1.0). We filtered the event files to remove contamination by soft protons with the `espfilt` task (screened exposure times are shown in Table 1). Images and spectra were produced by selecting events with FLAG = 0 and PATTERN ≤ 4, 12 for pn and MOS cameras, respectively. The images were background-subtracted by adopting the double subtraction procedure described in Miceli et al. (2017). For the double subtraction, we used the Filter Wheel Closed (FWC) and Blank Sky (BS) files available at the *XMM-Newton* ESAC repository[1][2]. We produced EPIC mosaicked images by adopting the `emosaic` SAS task. We corrected the images for vignetting and produced count-rate maps by dividing the superposed EPIC images by the associated superposed exposure maps (obtained with the `eexpmap` task). The pn exposure maps were multiplied by the ratio of the pn/MOS effective areas, to yield MOS-equivalent superposed count-rate maps. Count-rate maps were then smoothed adaptively through the `asmooth` task. Spectra were extracted with the `evselect` task, while the arf and rmf files were produced with the arfgen and rmfgen tasks, respectively. We adopted the `evigweight` task for the vignetting correction. The *Chandra* data were analyzed with CIAO (v4.13), using CALDB (v4.9.4). The data were reprocessed with the chandra_repro task. Flux images of *Chandra* data were obtained by combining the two observation reported in Table 1 with the CIAO task `merge_obs`. The *Spitzer*/MIPS data analysis was performed with the MOPEX package (v 18.5.0), which we adopted to produce 24 μm mosaic images, and to extract point sources from BCD-level data for each observation. An amount of 2114 frames were mosaicked for each observation in 24 μm band.

The spectral analysis was performed using XSPEC (v12.11.1d, Arnaud 1996). Spectra include 20 counts per channel for each data set (*XMM-Newton* EPIC-pn/MOS1/MOS2 and *NuSTAR* FPMA/FPMB).

3. Results

3.1. Image analysis

In order to constrain the origin of the nonthermal X-ray emission in the interaction region between the southwestern limb of SN 1006 and the atomic cloud we first focused on the Fe Kα emission line. Figure 2 shows the *NuSTAR* (FPMA and FPMB summed) count image of the southwestern limb of SN 1006 in the 6.12−6.96 keV band. Beyond the emission from the shell, which is mainly associated with the nonthermal continuum (e.g., Miceli et al. 2009), an isolated knot (which can be called knot1) can be spotted outside the forward shock, centered approximately at $\alpha = 15^h\,01^m\,30.4^s$, $\delta = -42°\,06'\,10.9''$. The knot is well within the atomic cloud interacting with SN 1006 (see Fig. 2), approximately 2 pc upstream with respect to the shock front (assuming a distance of 2.2 kpc for SN 1006), and its size is comparable to the size of the telescope point-spread function (PSF) of *NuSTAR*.

Motivated by the results obtained with the *NuSTAR* data, we also inspected the *XMM-Newton* and *Chandra* data to exploit the large *XMM-Newton* effective area in the soft X-ray band and the superior spatial resolution provided by *Chandra*. Figure 3 shows the *XMM-Newton* (upper panels) and *Chandra* (lower-left panel) maps of the knot region in the 1–7 keV band. Both in the *XMM-Newton* and *Chandra* maps, we identified a small source[3], with center coordinates: $\alpha = 15^h\,01^m\,34.2^s$ and $\delta = -42°\,06'\,22.8''$ (indicated by a green circle in Fig. 3), well within the area corresponding to the *NuSTAR* PSF (marked by a red circle in the figure).

To determine whether the source is point-like or extended, we extracted the radial profile of its surface brightness and compared it with simulated PSF data for both *XMM-Newton* and *Chandra* (including *Chandra* observations from both 2003 and 2012). The *Chandra* PSF was obtained with the MARX software (v. 5.5.1), while the *XMM-Newton* PSF was produced with the task psfgen. The radial profiles of the source surface brightness are shown in Fig. 4. While the poor PSF of *XMM-Newton* means we were unable resolve the source, we still observed a significant deviation from the PSF radial profile in the 2003 and 2012 *Chandra* data, (i.e., the one expected for point-like sources). We estimated the extension of the source by carrying out simulations (with MARX) Gaussian profiles for the source surface brightness and exploring different values for the sigma, namely, $\sigma = 2''$, $\sigma = 3''$, $\sigma = 4''$. We find that the observed profile is well reproduced ($\chi^2 = 21.4$, with 9 d.o.f.) by the Gaussian with $\sigma = 3''$ (see right panel of Fig. 4), while the Gaussians with $\sigma = 2''$ and $\sigma = 4''$ offer a poorer description of

[1] https://www.cosmos.esa.int/web/xmm-newton/filter-closed

[2] http://xmm-tools.cosmos.esa.int/external/xmm_calibration//background/bs_repository/blanksky_all.html

[3] The source is 2CXO J150134.1−420620 in the *Chandra* catalog.

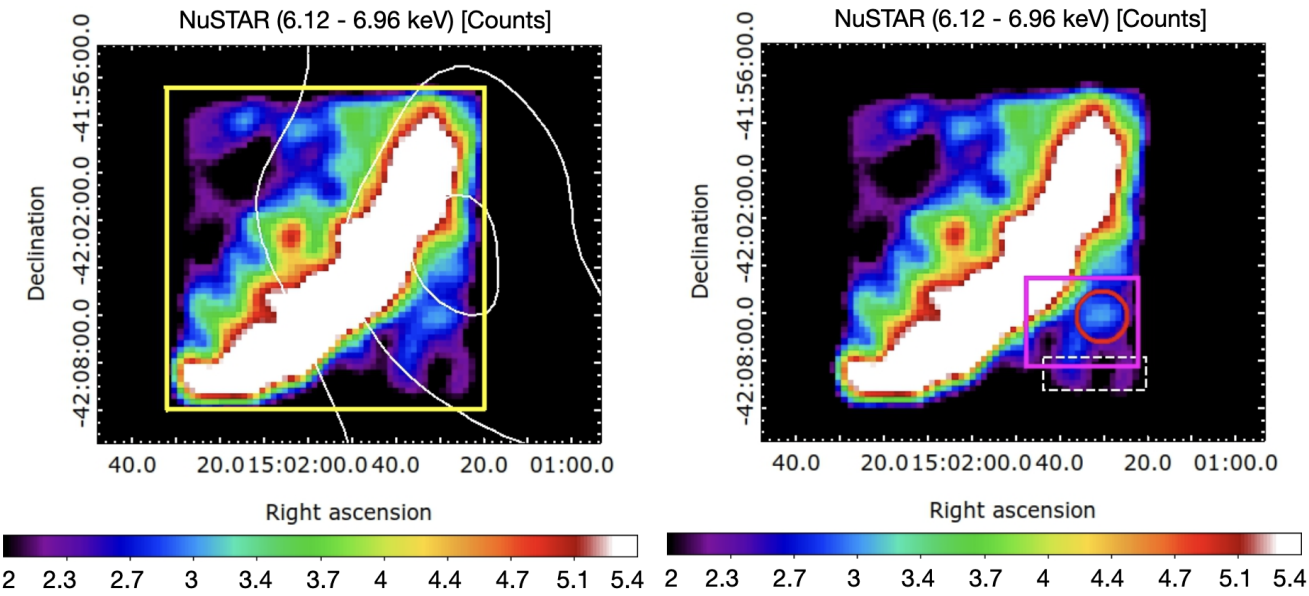

Fig. 2. *NuSTAR* observation of the southwestern part of SN 1006 in linear scale obtained as the sum of FPMA and FPMB in the 6.12−6.96 keV band. The pixel size is 14.7″. Left panel shows, in white, the contour levels of the column density (Fig. 1). The red circle on the right shows the region selected for spectral analysis of knot1 and the white dashed rectangle is the background region. The magenta box shows the field of view of the three panels in Fig. 3.

the data ($\Delta\chi^2 = 6.6$ and $\Delta\chi^2 = 2.5$, respectively)[4]. Our results point toward an extended X-ray source, with a radius of approximately 3″, corresponding to $\sim 10^{17}$ cm at a distance of 2.2 kpc. The extended X-ray knot which we revealed in the *XMM-Newton* and *Chandra* data may be associated with the *NuSTAR* excess, which we spotted in the Fe K band, considering the PSF of the *NuSTAR* telescope.

We also looked for an optical/IR counterpart of the extended X-ray knot. We did not find any optical counterpart within 15″ from the center of the *Chandra* source by inspecting the ESO Online Digitized Sky Survey. On the other hand, we clearly identified the IR counterpart of the source, detected with *Spitzer* (source ID 2530 in the MOPEX/APEX catalog). Figure 3 (lower-right panel) shows the *Spitzer*/MIPS image (in MJy sr^{-1}) at 24 μm, and the source position is indicated by the green circle. The IR flux of the source at 24 μm is $F_{\rm MIPS} = (6.0 \pm 1.5) \times 10^{-14}$ erg s^{-1} cm^{-2}.

3.2. Spectral analysis

The spectra were extracted from a circular region with radius $R_{\rm XMM} = 22.0''$, $R_{\rm Nu} = 65.0''$ and the center coordinates are: $\alpha = 15^{\rm h}\,01^{\rm m}\,34.2^{\rm s}$, $\delta = -42^\circ\,06'\,22.8''$ and $\alpha = 15^{\rm h}\,01^{\rm m}\,30.4^{\rm s}$, $\delta = -42^\circ\,06''\,10.9''$ for *XMM-Newton* and *NuSTAR* data, respectively (note: the *Chandra* spectra were not analyzed because of their poor statistics). The background regions are shown in Fig. 2b (white rectangle) and Fig. B.1 (yellow ellipse) for *NuSTAR* and *XMM-Newton*, respectively. The spectral analysis was performed on EPIC-pn data in the 0.5−7.5 keV band, on EPIC-MOS1/MOS2 data in the 0.5−5 keV band, and on *NuSTAR* data in the 3−10 keV band. The background spectra were extracted from nearby regions without visible point-like sources. *NuSTAR* spectra clearly revealed the presence of an emission line at ∼6.5 keV.

Figure 5 shows the FPMA and FPMB spectra in the Fe K spectral band with the corresponding best fit model, consisting of a power law plus one Gaussian component. On the other hand, the Ne and Si emission lines at ∼0.89 keV and ∼1.89 keV, respectively, can be observed in the *XMM-Newton* spectrum (shown in Fig. 6). In the case where the *NuSTAR* knot in the Fe K band and the *Chandra*/*XMM-Newton* hard extended clump are believed to originate from the same source, we have expected the *NuSTAR* and *XMM-Newton* spectra to be effectively described by the same model simultaneously. We verified that this is indeed the case and the spectral model consists of a power law plus narrow Gaussian components. We also included the effects of the interstellar absorption (`tbabs` model within XSPEC) by fixing the interstellar column density at $N_{\rm H} = 8 \times 10^{20}$ cm^{-2} (Miceli et al. 2014), and a multiplicative constant to account for the cross-calibration factor between the two telescopes, which was left free to vary between 0.9 and 1.1 (in agreement with Madsen et al. 2017) in the fitting process. Figure 7 shows all the spectra with the corresponding best-fit models. Best fit parameters are shown in Table 2, errors are at the 68% confidence level. The global continuum can be accurately represented by a relatively flat power-law function, with photon index $\Gamma = 1.4^{+0.5}_{-0.4}$; this is strongly suggestive of a non-thermal origin. We also detected Fe, Si and Ne line complexes with a statistical significance of 95.5%, 99.99%, and 99.0%, respectively.

4. Discussion

We identified an excess in the Fe emission line (with line centroid at approximately 6.5 keV) in the *NuSTAR* observations of the southwestern region of SN 1006. This excess is consistent with being associated with a small (∼3″) X-ray knot, visible with *Chandra* and *XMM-Newton*, whose spectrum shows a flat continuum and Si and Ne emission lines. The knot is located at a projected distance of ∼2 pc from the shell (Fig. 2), where the remnant interacts with an atomic cloud (Miceli et al. 2014, 2016) and also shows an IR counterpart, detected with *Spitzer* at

[4] We obtained similar results by assuming for the surface brightness a uniform disk with a radius of $r = 3''$, but with a slightly higher value of χ^2 (namely $\chi^2 = 26.1$).

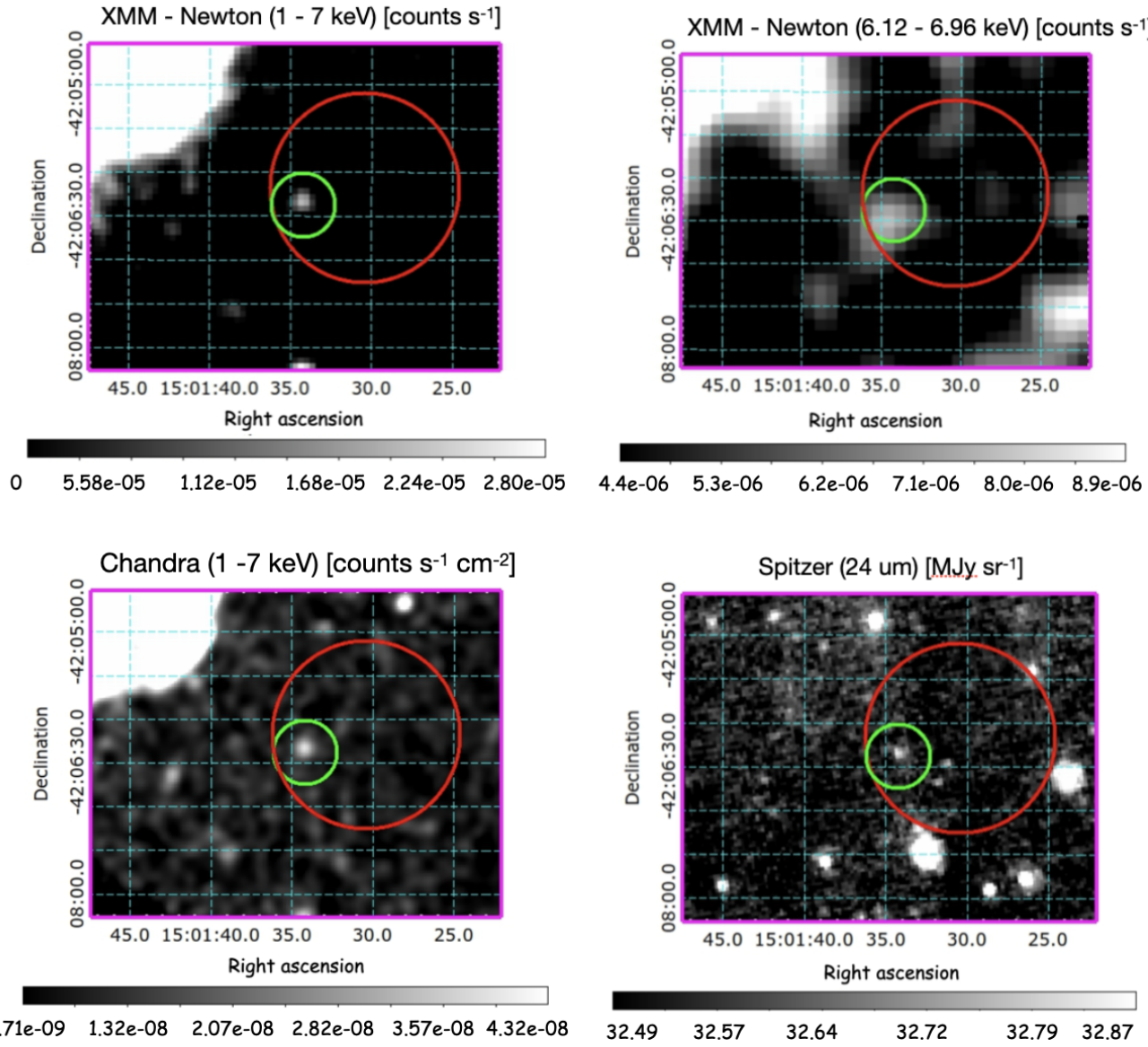

Fig. 3. *XMM-Newton*-EPIC count-rate map showing a close-up view of the southwestern limb of SN 1006 in the 1–7 keV band. Top-left panel: bin size of 4″. The red and green circles indicate the regions adopted to extract the *NuSTAR* and *XMM-Newton* spectra of knot1. The field of view corresponds to the magenta box in the right panel of Fig. 2. Top-right panel: same as the upper left panel in the 6.12−6.96 keV band, with bin size 8″. Lower-left panel: flux image of the same area in the 1–7 keV band (bin size 2″). Lower-right panel: IR emission of the same region, as observed with *Spitzer* at 24 μm.

24 μm. The origin of the source can be explained by two different scenarios. We discuss them separately.

4.1. Diffusion of low-energy cosmic rays

As mentioned in Sect. 1, Fe K emission line can be associated with LECRs diffusing from the shock of an SNR to a nearby dense cloud. We then investigated the possibility that particles (electrons and protons), accelerated in the southwestern limb of SN 1006 can produce the observed flux for the Fe line (i.e., $F_{\rm Fe} \sim 1.9 \times 10^{-7}$ photons s^{-1} cm^{-2}, see Table 2) by irradiating the southwestern atomic cloud. We assumed that LECRs have left the shock front of SN 1006 at the onset of its interaction with the neutral cloud. Miceli et al. (2016) estimated that the shock front reached the atomic cloud ~750 yr after the explosion; hence, LECRs have had $t_{\rm d} \sim 250$ yr to diffuse away from the acceleration site. The proton cross-section for the production of the Fe Kα line peaks at energies $E_{\rm p} \sim 10$ MeV (Tatischeff et al. 2012), corresponding to a proton speed of $v_{\rm p} \sim 0.14\,c$ (where c is the speed of light). We can then set an upper limit for the distance between 10 MeV protons and the acceleration site at the free-streaming value $L = t_{\rm d} v_{\rm p} \approx 10$ pc, which is larger than the projected distance between the X-ray emitting knot and the SN 1006 shock front (which is only 2 pc). In principle, LECRs may possibly be diffusing within the cloud. We estimated the expected flux of the Fe Kα line associated with cosmic-ray protons and electrons by following the same approach as Phan et al. (2020). The best fit for the multiwavelength data is shown in Fig. 8, where we tested different values of the power-law index δ in the equation for the cosmic-ray density (Eq. (1)):

$$n_{{\rm CR},i}(p_i) = A_i \left(\frac{p_i c}{\rm MeV}\right)^{-(\delta+2)} \exp\left[-\left(\frac{p_i}{p_i^c}\right)^{\beta}\right], \quad (1)$$

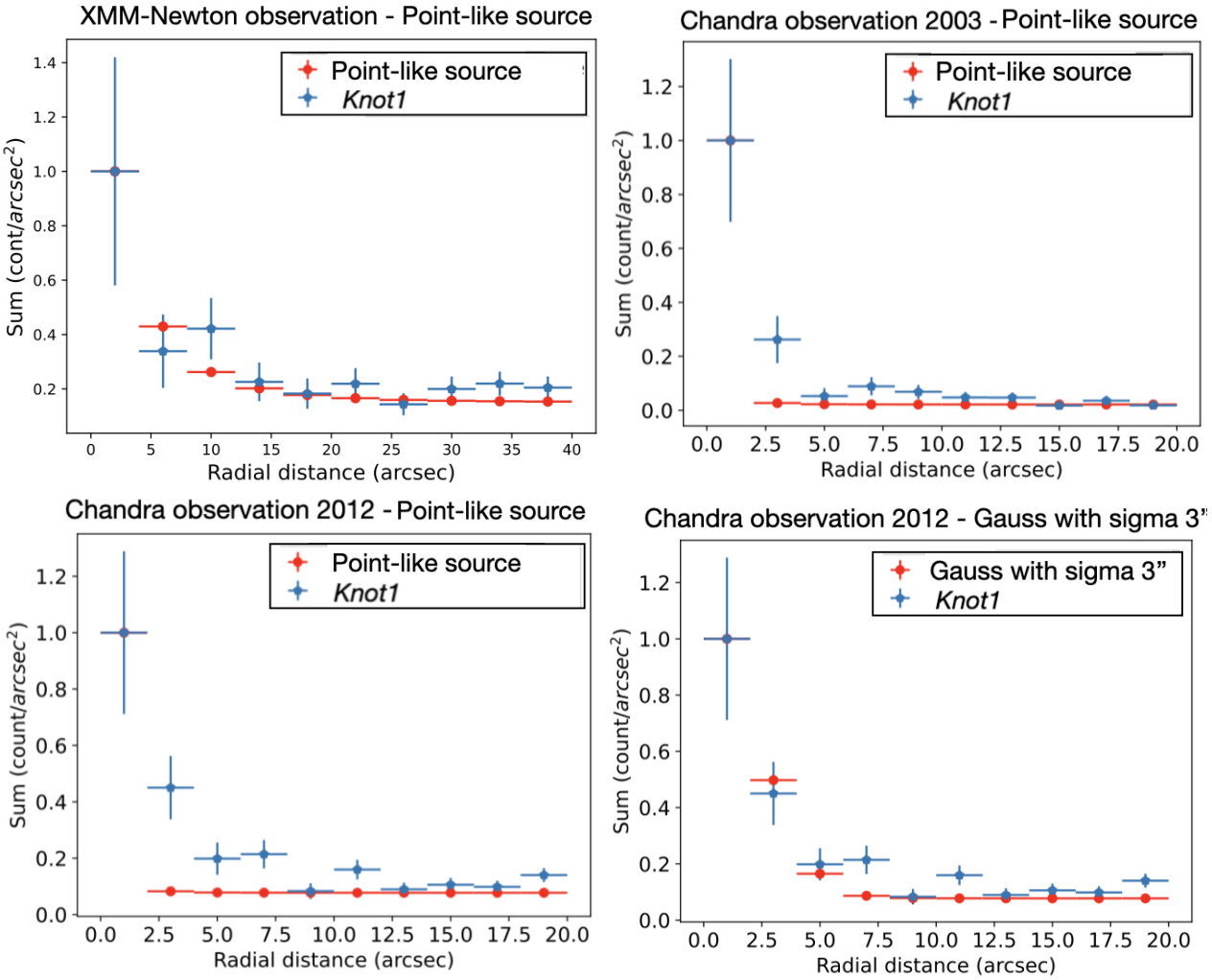

Fig. 4. *Upper-left panel*: comparison between the radial profiles of the knot1 surface brightness (blue crosses) and that of a simulated point-like source (red crosses, including the contribution of the background) for the *XMM-Newton* data. *Upper-right panel*: same as left panel, but for the *Chandra* 2003 observation. *Lower-left panel:* same as upper-right panel, but for the *Chandra* 2012 observation. *Lower-right panel*: same as lower-left panel, but for a simulated Gaussian profile with $\sigma = 3''$ (red crosses).

where i corresponds to the species of the CR particle (proton or electron), A_i is the normalisation factor, p_i is the momentum of the particle, δ is the power-law index, and p_i^c is the cut-off momentum. All the details on the model can be found in Appendix A.

The scenario including $\delta = 2.1$ seems to provide the best fit for the multiwavelength data (see Fig. 8). The Fe Kα line intensities expected from the CR protons and electrons are 3.4×10^{-10} cm^{-2} s^{-1} and 2.9×10^{-11}cm^{-2} s^{-1}, respectively. These values are 3 to 4 orders of magnitude lower than the observed line flux. The mass of the cloud would have to be higher by 3 or 4 orders of magnitude respectively, for the expected flux to match the observed value; this is unlikely, given the location of the remnant at $\sim$ 550 pc above the galactic plane. Hence, we can readily dismiss the case in which the Fe Kα line results from the interaction of LECR with the atomic cloud.

4.2. Fast ejecta fragment

Another scenario which can explain the X-ray emission of the source shown in Figs. 2 and 3 is based on nonthermal continuum and emission lines stemming from fast, metal-rich ejecta fragments in SNRs interacting with a dense ambient medium (B02, Bykov 2003). A supersonic fragment is preceded by a collisionless bow-shock that enables non-thermal particles to be shock-accelerated. Electrons with keV to MeV energies can diffuse back into the fragment and K-shell ionise neutral matter, resulting in Kα line emission. By solving a transport equation for non-thermal electrons, Bykov (2002) showed that even for conservative choices of the electron acceleration efficiency and diffusion coefficient, this model predicts observable fluxes of Kα X-rays. Bremsstrahlung from the non-thermal electrons contributes a rather hard continuum with a spectral index of $\approx$1.5.

Previous works on different remnants, e.g., IC 443 (Bocchino & Bykov 2003; Bykov et al. 2008) and Kes 69 (Bocchino et al. 2012), have shown an IR counterpart for X-ray emitting ejecta fragments interacting with interstellar clouds. The X-ray source in analysis shows a significant IR counterpart at 24 µm (lower-right panel of Fig. 3), which is in line with this scenario. In particular (as explained in Sect. 2), we detected a point-like source at $\alpha = 15^{\rm h}\,01^{\rm m}\,34.1825^{\rm s}$, $\delta = -42^\circ\,06'\,20.447''$, with a flux density of $6.0 \pm 0.5 \times 10^2$ µJy (corresponding to $F_{\rm MIPS} = 6.0 \pm 0.5 \times 10^{-14}$ erg s^{-1} cm^{-2} in the *Spitzer* 24 µm band, which ranges from 15 µm to 30 µm). Fine-structure lines of [FeII] (26 µm) might provide the main contribution to the flux in the *Spitzer* 24 µm band. By following

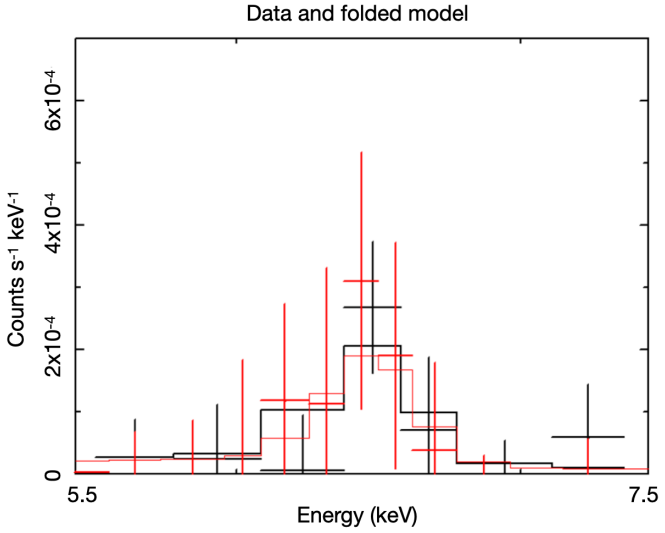

Fig. 5. *NuSTAR* FPMA (black) and FPMB (red) spectra of the knot1 in 5–7 keV band with the corresponding best-fit model.

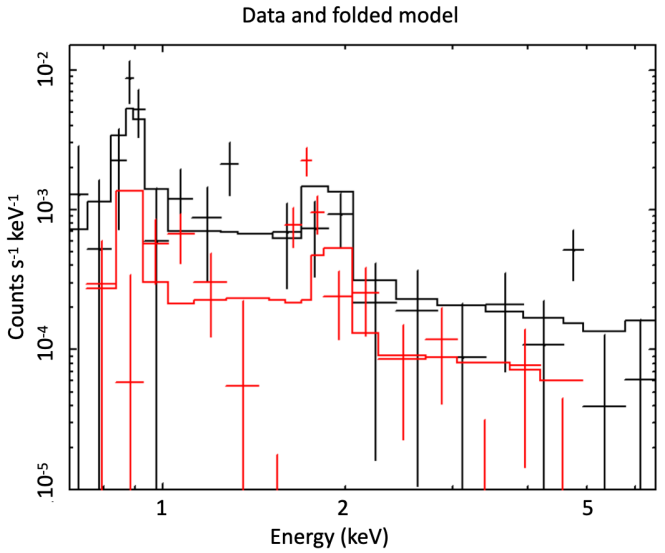

Fig. 6. *XMM-Newton* (EPIC-pn in black, MOS1+MOS2 in red) spectra of the knot1 with the corresponding best-fit model.

Hollenbach & McKee (1989), we can write the [FeII] (26 µm) line flux as

$$F_{26} \approx 2.4 \times 10^{-13} \frac{A}{10^2} \frac{n_{\rm knot}}{10^3} \frac{v_{\rm shk}}{10^2} \,{\rm erg\,cm^{-2}\,s^{-1}}, \quad (2)$$

where A is the angular area of the knot in units of arcsec^2, $n_{\rm knot}$ is the pre-shock density of the ejecta knot in units of cm^{-3}, and $v_{\rm shk}$ is the velocity of the shock moving in the knot in units of km s^{-1}. In this scenario, the ejecta knot is moving within the southwestern cloud, so we can consider: $v_{\rm shk}/v_{\rm bow} = \sqrt{n_{\rm cl}/n_{\rm knot}}$ (where $v_{\rm bow}$ is the bow shock velocity and $n_{\rm cl}$ is the cloud density). Therefore, from Eq. (2), we can write:

$$n_{\rm knot} = \left(\frac{F_{26}}{2.4 \times 10^{-13}} \frac{10^2}{A} \frac{10^3}{v_{\rm bow}} \frac{10^2}{\sqrt{n_{\rm cl}}} \right)^2, \quad (3)$$

where $F_{26} = F_{\rm MIPS}$, $n_{\rm cl} = 0.5\,{\rm cm^{-3}}$ (Miceli et al. 2016), and $A = \pi r^2$ ($r = 3''$, as explained in Sect. 3). assuming that the knot velocity lies in the plane of the sky, we set

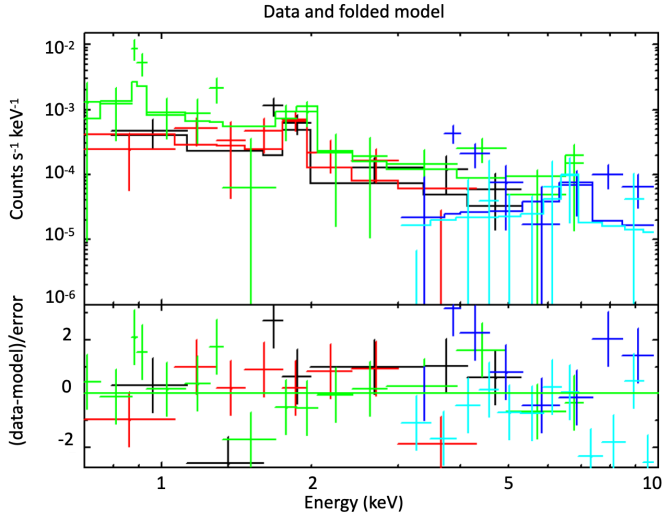

Fig. 7. *XMM Newton* (EPIC-MOS1 in black, EPIC-MOS2 in red, and EPIC-pn in green) and *NuSTAR* (FPMA in blue, FPMB in light blue) spectra of the knot1 with the corresponding best-fit models and residuals.

Table 2. Best-fit parameters for the spectral analysis of knot1.

Component	Parameter	Best fit value
Tbabs	$N_{\rm H}$	8×10^{20} cm^{-2}
powerlaw	Γ	$1.4^{+0.5}_{-0.4}$
Gauss1	E	$1.89^{+0.03}_{-0.02}$ keV
Gauss1	norm ($\times 10^{-7}$)	$2.6^{+0.8}_{-0.8}$ ph cm^{-2} s^{-1}
Gauss2	E	$6.52^{+0.08}_{-0.07}$ keV
Gauss2	norm ($\times 10^{-7}$)	$1.9^{+1.0}_{-1.0}$ ph cm^{-2} s^{-1}
Gauss3	E	$0.89^{+0.02}_{-0.02}$
Gauss3	norm ($\times 10^{-7}$)	$3.4^{+1.6}_{-1.6}$ ph cm^{-2} s^{-1}
	χ^2	151.19
	d.o.f.	101

Notes. Errors are at the 68% confidence level.

$v_{\rm bow} = 6000\,{\rm km\,s^{-1}}$, which is obtained by scaling the velocity of the shock in the southwestern limb of SN 1006 (about 5000 km s^{-1}, Winkler et al. 2014) by the factor $f = d_{\rm knot}/R_{1006}$, where R_{1006} and $d_{\rm knot}$ are the distances of the shock front and of the knot, respectively, from the center of the remnant. We then get $n_{\rm knot} = (431 \pm 64)\,{\rm cm^{-3}}$, corresponding to a mass of $M_{\rm knot} = (1.4 \pm 0.2) \times 10^{-3}\,M_\odot$, assuming solar abundances. We caution that Eqs. (2) and (3) were derived for a knot with solar abundances (Hollenbach & McKee 1989). Since the chemical composition strongly affects the efficiency of radiative cooling, then the temperature and density profile of the shock, a proper correction of Eqs. (2) and (3) for a pure-metal knot is difficult to evaluate. In this case, we need to assume that the mass of the knot is of the order of $10^{-3}\,M_\odot$.

The parameters derived for the X-ray and IR emitting knot are similar to those considered in B02, where the authors modeled the emission stemming from a fast moving ejecta fragment with radius $R \sim 3 \times 10^{16}$ cm and mass $M \sim 10^{-3}\,M_\odot$. In that case the knot is composed predominantly by oxygen, with $\sim 10^{-4}\,M_\odot$ of impurities (Si, S, Ar, Ca, Fe). B02 analyzed two different scenarios, namely (i) ejecta fragments moving in a dense (10^3 cm^{-3}) molecular cloud and (ii) in a low density medium (0.1 cm^{-3}).

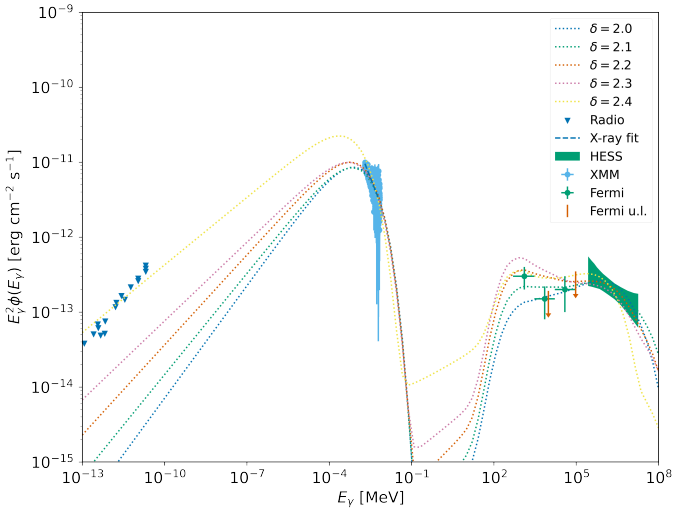

Fig. 8. Multiwavelength data fit with emissions from CR interactions for various δ .

In order to compare the emission predicted by B02 with that observed by us, we focused on the second scenario, where the density is similar to the density of the atomic cloud interacting with the southwestern part of SN 1006 ($n_{\rm cl} \sim 0.5\,{\rm cm}^{-3}$, Miceli et al. 2016). Indeed, according to B02, the X-ray flux is expected to increase with the ambient density, so the values predicted by B02 should be considered as lower limits for the case of SN 1006, where the ambient density is a factor of 5 higher.

Table 3 shows the comparison between the X-ray emission properties predicted by B02 and the results obtained with our spectral analysis of the knot interacting with the atomic cloud in the southwestern part of SN 1006. We found that the continuum emission is in good agreement with expectations. In particular, the photon index is <1.5 (as predicted in B02) and the X-ray luminosity (in the 4–10 keV band) is $>10^{30}\,{\rm erg\,s}^{-1}$, in agreement with expectations for knots larger than 10^{17} cm (see B02 for details). On the other hand, we observed a higher luminosity for the Si and Fe line complexes than those predicted by B02 for an O-rich knot. In particular, the results for the Si-line luminosity and the Fe-line luminosity are about 20 and 50 times greater than the expected values, respectively. This effect can be due to differences in the chemical composition of the ejecta knot since the knot in B02 contains only 10% of Si, S, Ar, Ca and Fe. In the case of knot1, the chemical composition suggests that it originates from the innermost part of the remnant (high-velocity Fe rich knots have been observed in type Ia supernovae, Diehl et al. 2014).

We have assumed the *NuSTAR* source to be associated with the same source observed in the *XMM-Newton*, *Chandra*, and *Spitzer* data. Nevertheless, our conclusions stay unaffected even if we remove this assumption and do not include the Fe line in the spectral fittings. In particular, we recovered the same flux and photon index as those previously obtained.

4.3. Proper motion

To verify the effective motion of the knot, we checked its proper motion using *Chandra* observations. We compared the data collected in 2012 (ObsID 13738 and 14424) and in 2003 (ObsID 4387) using an absolute coordinate system as in Winkler et al. (2014). We then run the tool `wavedetect` to find X-ray point-like sources in each observation and we ran `wcs match` to match the X-ray sources with their optical counterpart detected in the NOMAD catalog. Unfortunately, the limited number of counts available in both observations hamper the possibility of performing a robust analysis. The results are shown in Fig. 9. The knot seems to move from an initial position (2003, Fig. 9, top-left panel), to a final position (2012, Fig. 9 bottom-right panel) of 5 arcsec in the north-west direction. However, this is not confirmed by the 2004 and 2010 *XMM-Newton* observations, where no significant proper motion is detected (lower panels of Fig. 9). For the *XMM-Newton* analysis, we used the combined count-rate image taking into account pn, MOS1, MOS2. A new *Chandra* observation is necessary to provide a more reliable assessment of the proper motion of the source.

Table 3. Comparison between results found in this paper and predictions by B02.

Parameter	This paper	B02
Radius (cm)	1×10^{17}	3×10^{16}
Mass ($M_\odot$)	$(1.4\pm0.2)\times10^{-3}$	10^{-3}
Ambient density (cm^{-3})	0.5	0.1
Si luminosity (ph s^{-1})	1.6×10^{38}	6.7×10^{36}
Fe luminosity (ph s^{-1})	1.0×10^{38}	2.1×10^{36}
$L_{\rm X}$ (4−10 keV) (erg s^{-1})	3.5×10^{30}	$\gtrsim10^{30}$ [(a)]
Photon index	$1.4^{+0.5}_{-0.4}$	≤1.5

Notes. We calculated all of the luminosity from fluxes in Table 2 assuming a distance of 2.2 kpc. [(a)]Calculated for fragment larger than 10^{17} cm (B02).

4.4. Alternative interpretations

We cannot exclude the possibility that the source is not associated with SN 1006. The X-ray emission from knot1 could, in principle, have a galactic or an extragalactic origin. The significant extension of knot1 clearly points against a stellar origin or a compact object, thus making the galactic scenario unlikely. The Fe-Kα line and a flat continuum below 10 keV ($\Gamma < 2$) are indeed among the main characteristics of AGNs and Seyfert galaxies. Moreover, it has been found that some of them can show extended X-ray emission, such as in Arévalo et al. (2014), Bauer et al. (2015), Fabbiano et al. (2017, 2018a,b, 2019), Maksym et al. (2017), Jones et al. (2020) and Travascio et al. (2021). However, an optical counterpart should be visible, which is not the case for knot1, and no proper motion should be visible. The extragalactic catalogs do not provide any detection located at knot1.

5. Summary and conclusion

We analyzed the X-ray emission of the southwestern limb of SN 1006, where the remnant is interacting with an atomic cloud (Miceli et al. 2014, 2016). We used data from three different X-ray telescopes: *NuSTAR*, *XMM-Newton*, and *Chandra*.

We discovered an X-ray knot out of the shell (about 2 pc upstream of the shock front), which is clearly visible in the *XMM-Newton* and *Chandra* data and shows an IR counterpart, which we observed in the *Spitzer* MIPS 24 μm data. In a region compatible with the *Chandra* and *XMM-Newton* localization, the analysis of *NuSTAR* data indicates the presence of an X-ray source within the atomic cloud interacting with the southwestern

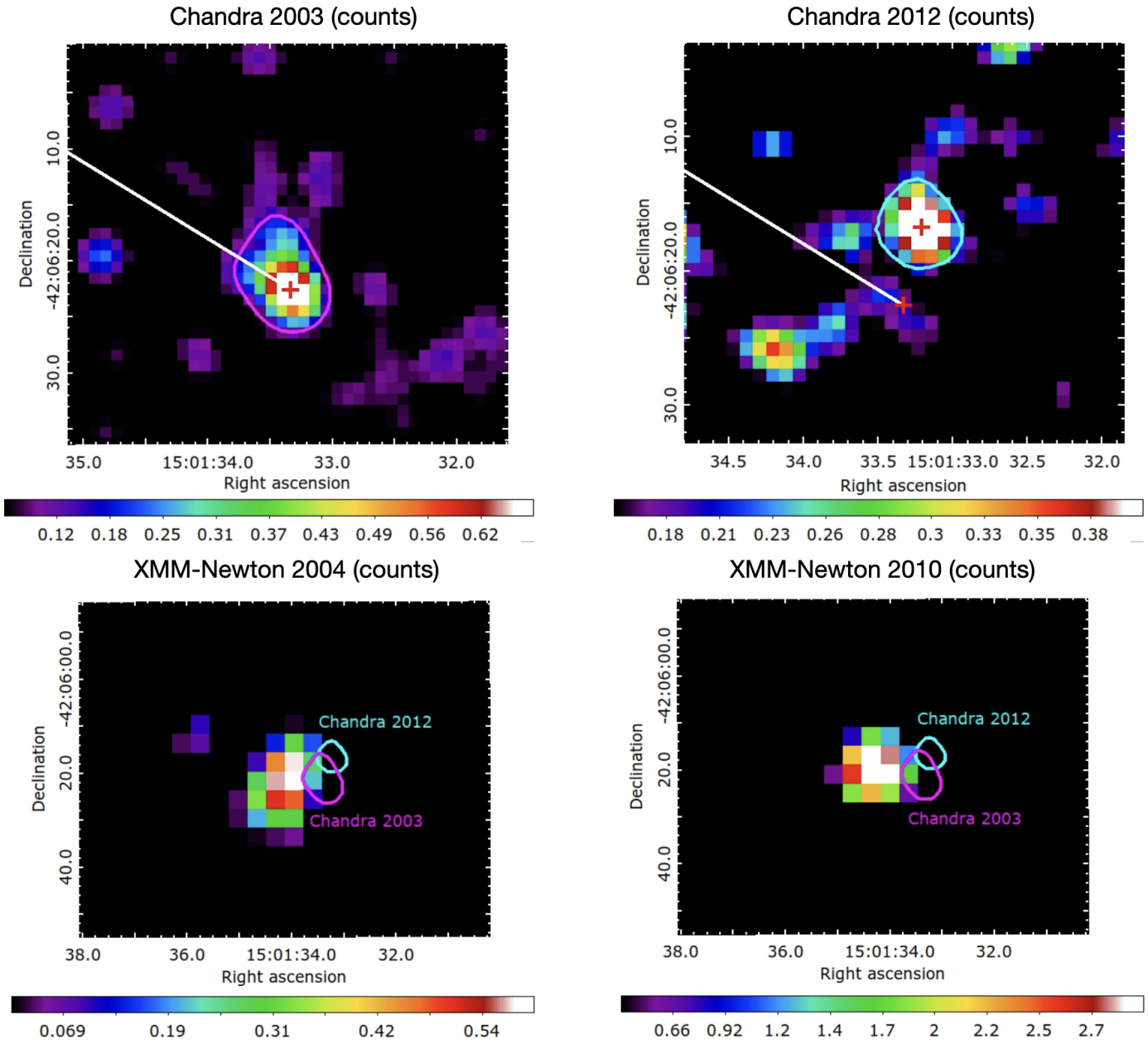

Fig. 9. *Chandra* counts image observed in 2003, shown in the top-left panel. The red point shows the position of the source and the white line indicates the direction to the center of the remnant. The magenta region marks the shape of the source. The top-right panel: *Chandra* counts image observed in 2012. The northern red point indicates the position of the source and he cyan region marks its shape. Bottom-left panel: *XMM-Newton* counts image observed in 2004. Bottom-right panel: *XMM-Newton* counts image observed in 2010. The magenta and the cyan regions in both the lower panels indicate the source detected with *Chandra* in 2003 and 2012, respectively.

limb of SN 1006 (Fig. 2) whose size is comparable with the PSF of the telescope. The combined analysis of *XMM-Newton* and *Chandra* observations, with their higher effective area and spatial resolution, allowed us to constrain the location and the extension of the source. As a result, we found a knot centered at $\alpha = 15^{h}\,01^{m}\,34.2^{s}$ and $\delta = -42^{\circ}\,06'\,22.8''$ with radius $R \sim 1 \times 10^{17}$ cm (assuming the same distance as SN 1006).

Spectral analysis of the X-ray knot shows three significant emission lines at: 0.89, 1.89 keV, and 6.5 keV (see Table 2 and Fig. 7) associated with Ne, Si, and Fe, respectively. With respect to their origins, we have considered two different scenarios:

1. Low-energy cosmic rays diffusing from the shock in the SW limb of SN 1006 to the atomic cloud produce non-thermal emission lines, especially the characteristic Fe-Kα line at 6.4 keV. However the CR spectra that best fit the multiwavelength observations of the SW limb produce a Fe-Kα line intensity that is several orders of magnitude lower than the observed intensity.
2. Fast ejecta fragments in SNR interacting with interstellar clouds produce IR emission and nonthermal X-ray emission, characterized by a hard continuum and emission lines. The presence of an IR counterpart for the isolated knot in SN 1006, together with its X-ray flux and spectral shape, are in good agreement with the predictions by B02. We report higher luminosities for the emission lines than those predicted by B02 and interpret this as the result of a different chemical composition of the ejecta knot. We estimated the physical parameters of the ejecta knot, finding a density of

$n_{\rm knot} = (431 \pm 64)\,{\rm cm}^{-3}$ and a mass of $M_{\rm knot} = (1.4 \pm 0.2) \times 10^{-3}\,M_{\odot}$.

Nonthermal emission from fast ejecta knots has been observed only in the core-collapse SNRs IC 443 (Bykov et al. 2008) and Kes 69 (Bocchino et al. 2012). This paper provides the first indication of an Ne, Si, Fe-rich fragment of ejecta in a Type Ia SNR. The proper motion is crucial to confirm that the knot1 is a fast ejecta knot associated with SN 1006.

Acknowledgements. This work was partially supported by the INAF mini-grant "X-raying shock modification in supernova remnants", V.H.M.P. acknowledges support from the Initiative Physique des Infinis (IPI), a research training program of the Idex SUPER at Sorbonne Université. This study was also partially supported by the LabEx UnivEarthS, ANR-10-LABX-0023 and ANR-18-IDEX-0001.

References

Acero, F., Ballet, J., & Decourchelle, A. 2007, A&A, 475, 883
Acero, F., Aharonian, F., Akhperjanian, A. G., et al. 2010, A&A, 516, A62
Acero, F., Lemoine-Goumard, M., Renaud, M., et al. 2015, A&A, 580, A74
Arévalo, P., Bauer, F. E., Puccetti, S., et al. 2014, ApJ, 791, 81
Arnaud, K. A. 1996, in Astronomical Data Analysis Software and Systems V, eds. G. H. Jacoby, & J. Barnes, ASP Conf. Ser., 101, 17
Bauer, F. E., Arévalo, P., Walton, D. J., et al. 2015, ApJ, 812, 116
Bocchino, F., & Bykov, A. M. 2003, A&A, 400, 203
Bocchino, F., Bykov, A. M., Chen, Y., et al. 2012, A&A, 541, A152
Bykov, A. M. 2002, A&A, 390, 327
Bykov, A. M. 2003, A&A, 410, L5
Bykov, A. M., Bocchino, F., & Pavlov, G. G. 2005, ApJ, 624, L41
Bykov, A. M., Krassilchtchikov, A. M., Uvarov, Y. A., et al. 2008, ApJ, 676, 1050
Caprioli, D., Haggerty, C. C., & Blasi, P. 2020, ApJ, 905, 2
Celli, S., Aharonian, F., & Gabici, S. 2020, ApJ, 903, 61
Cosentino, G., Jiménez-Serra, I., Tan, J. C., et al. 2022, MNRAS, 511, 953
Cristofari, P., & Blasi, P. 2019, MNRAS, 489, 108
Diehl, R., Siegert, T., Hillebrandt, W., et al. 2014, Science, 345, 1162
Dogel', V. A., & Sharov, G. S. 1990, A&A, 229, 259
Dubner, G. M., Giacani, E. B., Goss, W. M., Green, A. J., & Nyman, L. Å. 2002, A&A, 387, 1047
Fabbiano, G., Elvis, M., Paggi, A., et al. 2017, ApJ, 842, L4
Fabbiano, G., Paggi, A., Karovska, M., et al. 2018a, ApJ, 855, 131
Fabbiano, G., Paggi, A., Karovska, M., et al. 2018b, ApJ, 865, 83
Fabbiano, G., Siemiginowska, A., Paggi, A., et al. 2019, ApJ, 870, 69
Gabici, S. 2022, A&A Rev., 30, 4
Gabici, S., Aharonian, F. A., & Casanova, S. 2009, MNRAS, 396, 1629
Giuffrida, R., Miceli, M., Caprioli, D., et al. 2022, Nat. Commun., 13, 5098
Haggerty, C. C., & Caprioli, D. 2020, ApJ, 905, 1
Hollenbach, D., & McKee, C. F. 1989, ApJ, 342, 306
Jones, M. L., Fabbiano, G., Elvis, M., et al. 2020, ApJ, 891, 133
Kafexhiu, E., Aharonian, F., Taylor, A. M., & Vila, G. S. 2014, Phys. Rev. D, 90, 123014
Katsuda, S., Petre, R., Long, K. S., et al. 2009, ApJ, 692, L105
Katsuda, S., Long, K. S., Petre, R., et al. 2013, ApJ, 763, 85
Khangulyan, D., Aharonian, F. A., & Kelner, S. R. 2014, ApJ, 783, 100
Korreck, K. E., Raymond, J. C., Zurbuchen, T. H., & Ghavamian, P. 2004, ApJ, 615, 280
Li, J.-T., Ballet, J., Miceli, M., et al. 2018, ApJ, 864, 85
Long, K. S., Blair, W. P., & van den Bergh, S. 1988, ApJ, 333, 749
Madsen, K. K., Christensen, F. E., Craig, W. W., et al. 2017, J. Astron. Telesc. Instrum. Syst., 3, 044003
Maksym, W. P., Fabbiano, G., Elvis, M., et al. 2017, ApJ, 844, 69
Miceli, M., Bocchino, F., Iakubovskyi, D., et al. 2009, A&A, 501, 239
Miceli, M., Bocchino, F., Decourchelle, A., et al. 2012, A&A, 546, A66
Miceli, M., Acero, F., Dubner, G., et al. 2014, ApJ, 782, L33
Miceli, M., Orlando, S., Pereira, V., et al. 2016, A&A, 593, A26
Miceli, M., Bamba, A., Orlando, S., et al. 2017, A&A, 599, A45
Nobukawa, K. K., Nobukawa, M., Koyama, K., et al. 2018, ApJ, 854, 87
Nobukawa, K. K., Hirayama, A., Shimaguchi, A., et al. 2019, PASJ, 71, 115
Okon, H., Uchida, H., Tanaka, T., Matsumura, H., & Tsuru, T. G. 2018, PASJ, 70, 35
Petruk, O., Dubner, G., Castelletti, G., et al. 2009, MNRAS, 393, 1034
Phan, V. H. M., Gabici, S., Morlino, G., et al. 2020, A&A, 635, A40
Raymond, J. C., Korreck, K. E., Sedlacek, Q. C., et al. 2007, ApJ, 659, 1257
Reynolds, S. P. 1996, ApJ, 459, L13
Schlickeiser, R. 2002, Cosmic Ray Astrophysics (Berlin: Springer-Verlag)
Tatischeff, V., Decourchelle, A., & Maurin, G. 2012, A&A, 546, A88
Travascio, A., Fabbiano, G., Paggi, A., et al. 2021, ApJ, 921, 129
Winkler, P. F., Gupta, G., & Long, K. S. 2003, ApJ, 585, 324
Winkler, P. F., Williams, B. J., Reynolds, S. P., et al. 2014, ApJ, 781, 65
Xing, Y., Wang, Z., Zhang, X., & Chen, Y. 2019, PASJ, 71, 77
Zhang, S., Tang, X., Zhang, X., et al. 2018, ApJ, 859, 141
Zirakashvili, V. N., & Aharonian, F. 2007, A&A, 465, 695
Zirakashvili, V. N., & Aharonian, F. A. 2010, ApJ, 708, 965

Appendix A: Model for LECRs diffusing in the cloud

In principal, fitting the non-thermal emissions from both the shock in the SW limb and the cloud requires a propagation model to describe the escape of CRs from the shock regions into the cloud. Such a model, however, necessitates quite a few free parameters, such as the shape and normalization of the diffusion coefficient of CRs in these regions over a broad energy range from MeV to TeV. To avoid inflating the number of free parameters, we adopted a more simplified approach, which is to assume that the CR density is uniform both in the shock and in the cloud regions. This assumption has led to a conservative upper limit for our predictions of the Fe Kα emission induced by LECRs escaping from the shock. We went on to see that this upper limit is expected to be much lower than the observed Fe Kα emission and, thus, more complicated propagation model might not be required.

We estimated the expected flux of the Fe Kα line associated with cosmic ray protons and electrons by following the same approach as Phan et al. (2020). In all following equations, the mass and momenta of the particles are given in MeV, that is: $m_i c^2$ and $p_i c$ for a particle, i. In particular, we assume a CR density of the form:

$$n_{CR,i}(p_i) = A_i \left(\frac{p_i}{\mathrm{MeV}}\right)^{-(\delta+2)} \exp\left(-\left(\frac{p_i}{p_i^c}\right)^{\beta}\right), \tag{A.1}$$

where i corresponds to the species of the CR particle (proton or electron), v_i is the particle speed, A_i is the normalisation factor (MeV^{-3} cm^{-3}), p_i is the momentum of the particle, δ is the power-law index, and p_i^c is the cut-off momentum. The exponential β of the cut-off is equal to 1.0 for protons and 2.0 for electrons as suggested by Zirakashvili & Aharonian (2007) for electrons accelerated in shell-type supernova remnants. The parameters δ, A_i and p_i^c can be determined by fitting the available multiwavelength data:

- Radio data from the entire remnant (Reynolds 1996);
- *XMM-Newton* X-ray data from the SW limb (see Appendix B);
- γ-ray data from FERMI and *HESS* both from the SW limb (Xing et al. 2019, Acero et al. 2015, Acero et al. 2010).

Additionally, we fit the *XMM-Newton*/EPIC-pn spectrum of the southwestern limb of SN 1006 between 2 keV and 6 keV as:

$$F_{X-ray}(E) = 1.14 \times 10^{-2} \left(\frac{E}{keV}\right)^{-2.938} \mathrm{cm^{-2}\ s^{-1}\ keV^{-1}}. \tag{A.2}$$

The main contribution from CR protons is the γ-ray emission. Following Kafexhiu et al. (2014), the spectrum of γ rays Φ_γ (MeV^{-1} cm^{-3} s^{-1}) resulting from the p-p interactions of a proton intensity J_p (MeV^{-1} cm^{-2} s^{-1} sr^{-1}) can be expressed in the following way:

$$\Phi_\gamma(E_\gamma) = 4\pi n_H \int \frac{d\sigma}{dE_\gamma}(E_p, E_\gamma) J_p(E_p)\, dE_p. \tag{A.3}$$

We modeled leptonic γ-ray emission via inverse Compton (IC) scattering and relativistic Bremsstrahlung following Cristofari & Blasi (2019). The spectrum of IC γ-rays Φ_{IC} (MeV^{-1} cm^{-3} s^{-1}) resulting from an electron density N_e (MeV^{-1} cm^{-3}) and a seed photon field (T, κ) where T is the temperature and κ is the dilution factor, is expressed in the following way (Khangulyan et al. 2014):

$$\Phi_{IC}(E_\gamma) = \int \frac{dN_{iso}}{d\omega dt}(E_\gamma, E_e, T, \kappa) N_e(E_e)\, dE_e. \tag{A.4}$$

The spectrum of γ-rays resulting from relativistic Bremsstrahlung Φ_{Brem} (MeV^{-1} cm^{-3} s^{-1}) produced by an electron density N_e (MeV^{-1} cm^{-3}) is as follows (Dogel' & Sharov 1990):

$$\Phi_{Brem}(E_\gamma) = c n_H \int \sigma_{Brem}(E_\gamma, E_e) N_e(E_e)\, dE_e, \tag{A.5}$$

where σ_{Brem} is the related cross-section from Schlickeiser (2002).

CR electrons also contribute to the radio and X-ray domains through synchrotron emission. The spectrum of synchrotron emission Φ_{syn} (MeV^{-1} cm^{-3} s^{-1}) from an electron density N_e (MeV^{-1} cm^{-3}) in a magnetic field B_0 can be expressed in the following way (Celli et al. 2020):

$$\Phi_{syn}(E_\gamma) = \frac{\sqrt{3} e^3 B_0}{2\pi m_e \hbar E_\gamma} \int_0^\infty R\left(\frac{E}{E_c(E_e)}\right) N_e(E_e)\, dE_e, \tag{A.6}$$

where e is the elementary charge, m_e is the rest mass energy of the electron, and where $E_c = 0.07 \left(\frac{B_0}{mG}\right)\left(\frac{E_e}{TeV}\right)^2$ keV, where B_0 is the magentic field and E_e the kinetic energy of the electron. The function R from Zirakashvili & Aharonian 2010 is defined as:

$$R(x) = \frac{1.81 e^{-x}}{\sqrt{x^{-2/3} + (3.62/\pi)^2}}. \tag{A.7}$$

We calculated the γ-ray emission from protons and electrons and synchrotron emission from electrons from the southwestern shell and cloud. According to Miceli et al. (2016), we assumed a spherical cloud with radius $R_{cl} \approx 5.5 \times 10^{18}$ cm and mass $M_{cl} = 0.4\ \mathrm{M_\odot}$. The average gas density n_{cl} is 0.5 cm^{-3} (Miceli et al. 2016). The magnetic field B_{cl} is not precisely known but expected to be of the order of a few micro Gauss. We take B_{cl} to be 10 μG to maximise synchrotron emission. Following Cristofari & Blasi (2019), the radius R_{sh} is taken as 7.7 pc and the volume-filling factor ξ_f is 0.25 as we only consider the SW limb. The volume of this part of the shell is then $V_{sh} = (\xi_f/3)\pi R_{sh}^3$. The post-shock gas density n_{sh} is 0.16 cm^{-3} (Giuffrida et al. 2022). The magnetic field B_{sh} is 90 μG (Winkler et al. (2014)).

We tried fitting the γ-ray and X-ray data using various different CR spectral indices δ between 2.0 and 2.8. The radio data points were taken as upper limits as they were obtained from the entire remnant. Using the best-fit parameters for each spectral index, we computed the expected Fe Kα line intensities from all the different CR spectra.

The intensity of the Fe Kα line resulting from CR interactions can be expressed as:

$$I_{K\alpha}^i = \frac{M_{cl}}{4\pi d_s^2 m_{avg}} \int_{T_i^{th}}^\infty \sigma_{K\alpha}^i(E_i) v_i N_i(E_i)\, dE_i, \tag{A.8}$$

where i represents the species of the CR particle, $\sigma_{K\alpha}^i$ is the K-shell ionisation cross-section by CR species i (Tatischeff et al. 2012), which takes into account solar abundance of Fe ($\eta_{Fe} = 3\times 10^{-5}$), and $m_{avg} = 1.4 m_H$. The intensity was obtained assuming a minimum ionising energy of 10 keV.

The expected intensities from the CR spectra are a few orders of magnitude lower than the measured Fe Kα line intensity. We also estimated the corresponding cloud mass to obtain the measured intensity based on these spectra. These values $I_{K\alpha}^i$ (photons cm^{-2}.s^{-1}) and the expected M_{cl} ($M_\odot$) are given in Table A.1.

Table A.1. Multiwavelength fit parameters normalisation A_i (MeV^{-3} cm^{-3}) and momentum cut-off p_i^c (MeV) for various CR spectral indices δ and corresponding Fe Kα line intensities (photons cm^{-2}s^{-1}).

δ	CR species	A_i	p_i^c	$I_{K\alpha}^i$
2.0	p / e$^-$	2×10^{-5} / 10^{-9}	2×10^8 / 2×10^7	1.3×10^{-10} / 5.1×10^{-12}
2.1	p / e$^-$	9×10^{-5} / 5×10^{-9}	5×10^8 / 2×10^7	3.4×10^{-10} / 2.9×10^{-11}
2.2	p / e$^-$	4×10^{-4} / 3×10^{-8}	5×10^8 / 2×10^7	8.7×10^{-10} / 2.0×10^{-10}
2.3	p / e$^-$	1.5×10^{-3} / 1.5×10^{-7}	10^9 / 2×10^7	1.9×10^{-9} / 1.1×10^{-9}
2.4	p / e$^-$	2×10^{-3} / 2×10^{-6}	10^9 / 1.5×10^7	1.5×10^{-9} / 1.7×10^{-8}
2.5	p / e$^-$	7×10^{-3} / 5×10^{-6}	10^9 / 2×10^7	3.1×10^{-9} / 4.9×10^{-8}
2.6	p / e$^-$	1×10^{-2} / 2.5×10^{-5}	10^9 / 2×10^7	2.7×10^{-9} / 2.9×10^{-7}
2.8	p / e$^-$	3×10^{-2} / 7×10^{-4}	10^9 / 2×10^7	2.9×10^{-9} / 1.1×10^{-5}

Appendix B: *XMM-Newton* observations in the SW limb

Figure B.1 shows the *XMM-Newton* flux image in counts/s of the southwestern limb of SN 1006. The region in black has been used to extract the spectrum useful to fit the X-ray data in Sect. 4.1. We also explored different background regions and verified that the best-fit values do not depend on this aspect specifically.

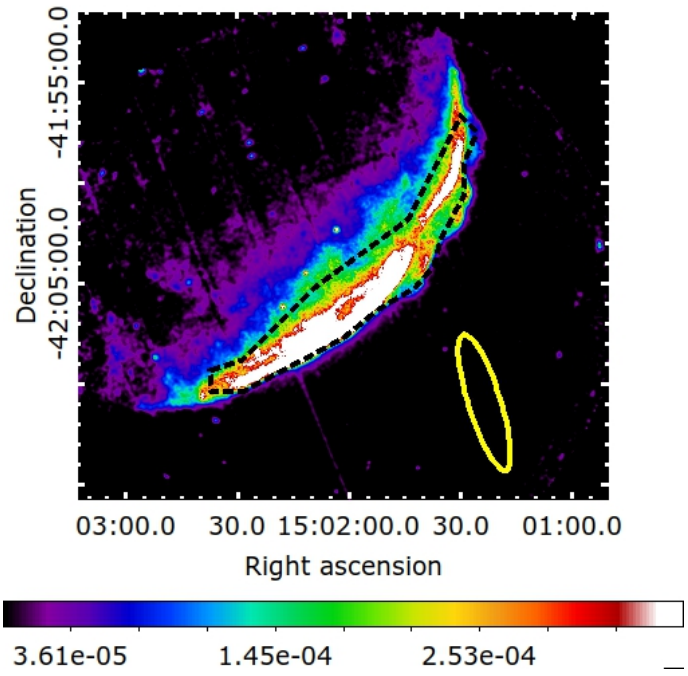

Fig. B.1. *XMM-Newton* flux image in counts/s of the SW limb of SN 1006. The black-dashed line shows the region useful for the X-ray data analysis from the SW limb. The yellow region marks the background region used to extract the EPIC-pn spectrum.